Magnetic-Electrical Synergetic Control of Non-Volatile States in Bilayer Graphene-CrOCl Heterostructures

Shimin Cao, Runjie Zheng, Cong Wang, Ning Ma, Mantang Chen, Yuanjun Song, Ya Feng, Tingting Hao, Yu Zhang, Yaning Wang, Pingfan Gu, Kenji Watanabe, Takashi Taniguchi, Yang Liu, X. C. Xie, Wei Ji,* Yu Ye,* Zheng Han,* and Jian-Hao Chen*

Anti-ferromagnetic insulator chromium oxychloride (CrOCl) has shown peculiar charge transfer and correlation-enhanced emerging properties when interfaced with other van der Waals conductive channels. However, the influence of its spin states to the channel material remains largely unknown. Here, this issue is addressed by directly measuring the density of states in bilayer graphene (BLG) interfaced with CrOCl via a high-precision capacitance measurement technique and a surprising hysteretic behavior in the charging states of the heterostructure is observed. Such hysteretic behavior depends only on the history of magnetization, but not on the history of electrical gating; it can also be turned off electrically, providing a synergetic control of these non-volatile states. First-principles calculations attribute this observation to magnetic field-controlled charge transfer between BLG and CrOCl during the phase transition of CrOCl from antiferromagnetic (AFM) to ferrimagnetic-like (FiM) states. This magnetic-electrical synergetic control mechanism broadens the scope of proximity effects and opens new possibilities for the design of advanced 2D heterostructures and devices.

1. Introduction

CrOCl, first synthesized at 1961,[1] has long been overlooked as a conventional low-symmetry van der Waals anti-ferromagnetic insulator until recently, when emerging phenomena including robust quantum Hall states,[2] correlated insulating state,[3] and carrier polarity reconfiguration,[4] have been discovered for van der Waals channels interfaced with CrOCl. Heterostructures of CrOCl with van der Waals channels such as single layer graphene (SLG),[2] bilayer graphene (BLG),[3] and transition metal dichalcogenides[4] have shown peculiar mobility-preserving and correlation-enhancing charge transfer properties. However, previous works have focused solely on transport (resistance) measurements which are naturally

S. Cao, R. Zheng, N. Ma, M. Chen, Y. Liu, X. C. Xie, J.-H. Chen
International Center of Quantum Materials
School of Physics
Peking University
Beijing 100871, P. R. China
E-mail: chenjianhao@pku.edu.cn

S. Cao, Y. Song, Y. Feng, T. Hao, Y. Zhang, J.-H. Chen
Beijing Academy of Quantum Information Sciences
Beijing 100193, P. R. China

C. Wang, W. Ji
Beijing Key Laboratory of Optoelectronic Functional Materials & Micro-Nano Devices
School of Physics
Renmin University of China
Beijing 100872, P. R. China
E-mail: wji@ruc.edu.cn

C. Wang, W. Ji
Key Laboratory of Quantum State Construction and Manipulation (Ministry of Education)
Renmin University of China
Beijing 100872, P. R. China

Y. Wang
Shenyang National Laboratory for Materials Science
Institute of Metal Research
Chinese Academy of Sciences
Shenyang 110016, P. R. China

P. Gu, Y. Ye
School of Physics
Peking University
Beijing 100871, P. R. China
E-mail: ye_yu@pku.edu.cn

K. Watanabe, T. Taniguchi
National Institute for Materials Science
Namiki 1-1, Tsukuba, Ibaraki 305-0044, Japan

X. C. Xie
Institute for Nanoelectronic Devices and Quantum Computing
Fudan University
Shanghai 200433, P. R. China

X. C. Xie, J.-H. Chen
Hefei National Laboratory
Hefei 230088, P. R. China

Z. Han
State Key Laboratory of Quantum Optics and Quantum Optics Devices
Institute of Opto-Electronics
Shanxi University
Taiyuan 030006, P. R. China
E-mail: zhenghan@sxu.edu.cn

J.-H. Chen
Key Laboratory for the Physics and Chemistry of Nanodevices
Peking University
Beijing 100871, P. R. China

**ADVANCED
SCIENCE NEWS**

www.advancedsciencenews.com

**ADVANCED
MATERIALS**

www.advmat.de

difficult in characterizing subtle changes in carrier density near the band gap of the channel (details in Figure S12, Supporting Information); indeed, previous works has not shown any effects of magnetic order in CrOCl to the van der Waals channels, due to the relatively weak influence on resistance of the channel from the spin orderings in CrOCl.[3]

In this work, we present quantum capacitance data for heterostructures composed of BLG and CrOCl (BLG-CrOCl).[2,3,5] An exotic correlated insulating state is confirmed from the measured density of states (DOS) of BLG, which is attributed to charge transfer and interfacial interactions between BLG and the localized surface states in CrOCl.[3] With the heterostructure magnetized and demagnetized by a sweeping perpendicular magnetic field $B_\perp$ between 0 and 6 T, hysteresis in the DOS versus $B_\perp$ is observed near the conduction and valence band edges of the BLG. Maximum hysteresis is found for $B_\perp$ between 3T and 4T in the magnetic field sweeping loop, which is consistent with the magnetic field-driven antiferromagnetic to canted-antiferromagnetic phase transition in CrOCl.[6] The hysteresis appears for temperatures below ≈13 K, which is the same as the Néel temperature T_N = 13.5 K in CrOCl.[6,7] Furthermore, the hysteresis is confirmed to be unaffected by the history of electrostatic gating on the heterostructure, indicating a pure magnetic origin. By electrically driving the BLG channel away from the transition region, such hysteretic behavior can be turned off, providing a synergetic control of these nonvolatile states. Based on density functional theory (DFT) calculations of the energy band structure of CrOCl with different magnetic orders, the experimental data can be understood as magnetic field-controlled charge transfer between BLG and CrOCl. This result highlights an example of synergetically controlled charging states in 2D material heterostructures and unveils the potential for a new mechanism of non-volatile information storage.

2. Results

2.1. Device Design and Characterization

CrOCl belongs to the MOX family of crystals (M = Ti, V, Cr, Fe; X = Cl, Br) with the space group P_{mmn}[1] and has been reported to be air stable down to the monolayer limit.[5] Each CrOCl monolayer consists of a Cr−O sheet sandwiched between two layers of Cl atoms in the a-b plane (see **Figure 1a,b**), and such monolayers stack along the c axis to form bulk CrOCl. The magnetic moments of the crystal are located on the Cr atoms (Figure 1c), and a first-order antiferromagnetic phase transition occurs at a Néel temperature of T_N = 13.5 K.[6,7] The spins along the a axis coupled ferromagnetically, while the spins along the b axis formed a 1 × 4 staggered Ising-like antiferromagnetic structure with zero net magnetic moment (Figure 1c, upper panel). When the applied perpendicular magnetic field is >3 T, a spin flop transition occurs[6] where the spins become canted toward the c axis (Figure 1c, middle panel). With further increase in the magnetic field, a second phase transition occurs in the spin structure, and a 1 × 5 staggered Ising-like antiferromagnetic structure with a finite net magnetic moment emerges (Figure 1c lower panel), giving rise to nonzero magnetization in the crystal.[7]

Since the valence band edge of CrOCl is ≈5.5 eV from the vacuum energy level,[8] which is larger than that of BLG (4.7 eV),[9] charge transfer is expected when a heterostructure is formed between CrOCl and BLG, as illustrated in the inset of Figure 1d. Indeed, previous studies on the in-plane resistance of single-layer graphene-CrOCl (SLG-CrOCl)[2] and BLG-CrOCl[3] heterostructures revealed peculiar electric field-tunable charge transfer between SLG/BLG and CrOCl. Here, we present quantum capacitance measurements of a BLG-CrOCl heterostructure, which revealed a novel magnetically tunable non-volatile charge transfer mechanism in BLG-CrOCl. The device and measurement schematics are depicted in Figure 1d. The dual-gated BLG devices are capped with hexagonal boron nitride (h-BN) on top and with CrOCl underneath. Exfoliation of high-quality Bernal-stacked BLG, thin CrOCl, and h-BN flakes from bulk crystals was completed under ambient conditions, with the resulting flakes placed onto a sapphire substrate via dry transfer methods[10] to reduce parasitic capacitance. Since CrOCl is highly insulating at temperatures below 200 K,[2] it serves as an ideal bottom dielectric layer with a dielectric constant of $\epsilon_{COC} \approx 4.9$[2,3] in our low-temperature (<20 K) measurement.

The circuit for the measurement is depicted in Figure 1d, where the changes in the DOS of the BLG in the BLG-CrOCl heterostructure were characterized by its capacitance C_{DUT}. Specifically, a single-arm capacitor bridge circuit was used to reduce the influence of parasitic capacitance in the transmission line;[11] two AC inputs, V_x and V_{REF}, are applied to the two ends of the capacitance bridge. The key components of this capacitor bridge were the BLG-CrOCl-graphite capacitor C_{DUT} and a reference capacitor C_R. When $V_x/V_{REF} = C_{DUT}/C_R$, this bridge is balanced, and will produce a zero output voltage V_{OUT}. Considering the finite noise in the system, the zero point will manifest itself as a minimum point in the $|V_{OUT}|$ versus V_{REF}/V_x curve (Figure 1e). As the DOS of the BLG is tuned via the DC top gate voltage V_{TG} or bottom gate voltage V_{BG}, C_{DUT} changes, and the minimum point of $|V_{OUT}|$ will move along the axis of V_{REF}/V_x. Here

$$C_{DUT}^{-1} = C_Q^{-1} + C_G^{-1} \tag{1}$$

where C_Q is the quantum capacitance and C_G is the parallel-plate geometric capacitance of the BLG-CrOCl-graphite device. The density of states of the BLG can then be calculated via the relation $dn/d\mu = C_Q/e^2$. More details of the measurement technique are provided in the Methods section.

Equation (1) implies that the quantum capacitance signal becomes significant when $C_Q \ll C_G$; thus, the precision capacitance measurement technique is most sensitive for materials with a low DOS, including Dirac materials,[12] intrinsic semiconductors,[13] quantum Hall[12a]/quantum spin Hall[14]/quantum anomalous Hall insulators[15] and correlated insulators.[16] This is complementary to the resistance measurement, where high resistance arises from a diminishing DOS is difficult to measure; in the situation of a high resistance bulk co-exists with conductive edges (e.g., in quantum Hall[12a]/quantum spin Hall/[14]quantum anomalous Hall insulators),[15] direct characterization of the insulating state by resistance measurement becomes impossible. Thus, we used a precision capacitance measurement technique to explore the peculiar insulating state

**ADVANCED
SCIENCE NEWS**

www.advancedsciencenews.com

**ADVANCED
MATERIALS**

www.advmat.de
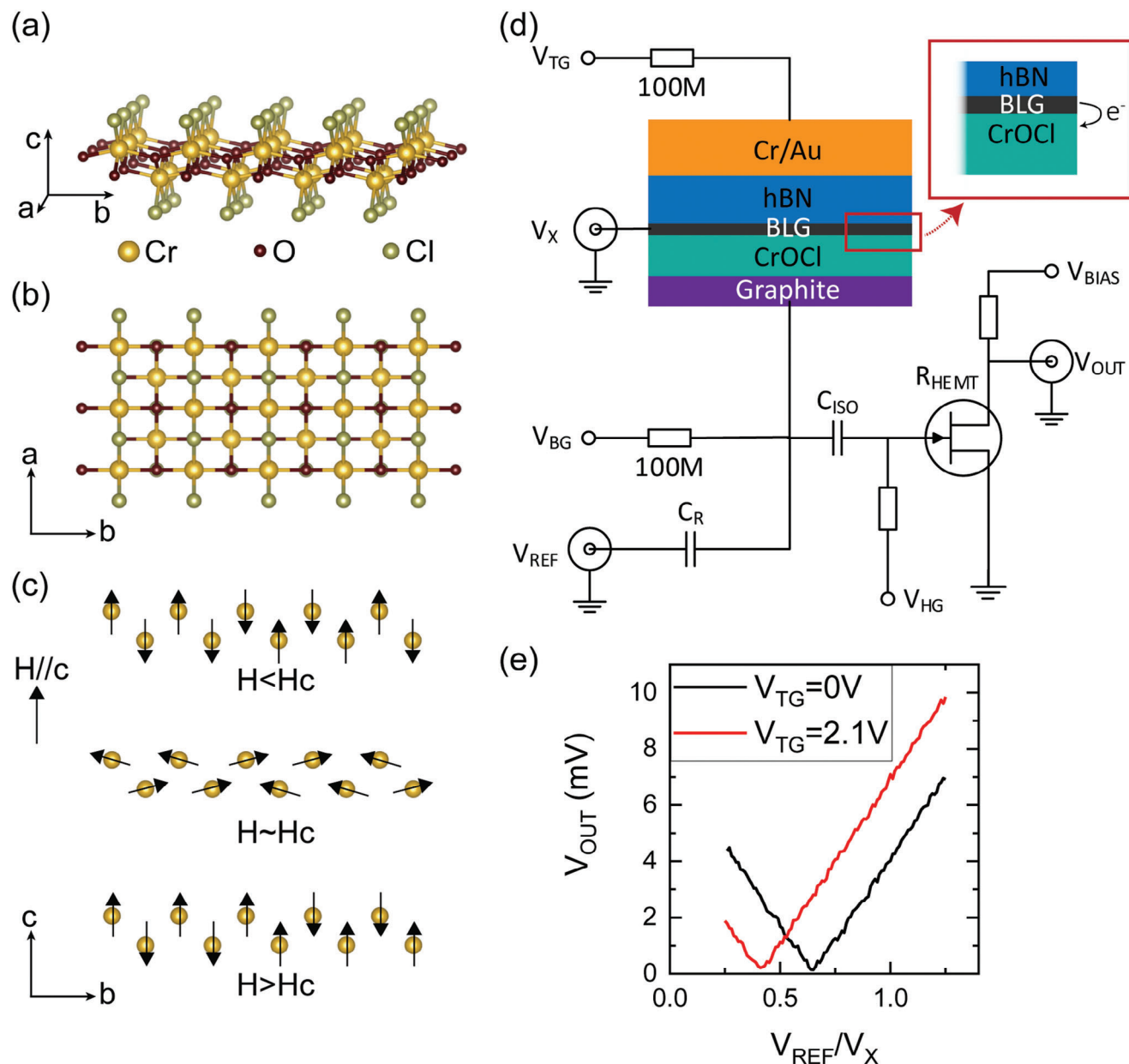
Figure 1. Bilayer graphene and CrOCl heterostructure (BLG-CrOCl) and capacitance measurement configuration. a,b) Atomic structure of antiferromagnetic insulator CrOCl. c) The low-temperature magnetic structure of CrOCl. d) Device structure and capacitance measurement circuit of BLG-CrOCl. Inset: illustration of charge transfer between BLG and CrOCl. e) Output voltage dependence on reference voltage of the single arm bridge in metallic and insulating states, respectively.

of the BLG-CrOCl heterostructure,[3] as well as the transition between the insulating state and the conductive state of the sample.

2.2. Charge Transfer-Induced Insulating State in BLG-CrOCl

Figure 2a presents a 2D diagram of C_{DUT} normalized to C_G, where the x- and y-axes are the total carrier density of the heterostructure $n_{total} = [C_{bg}(V_{bg} - V_{bg}^0) + C_{tg}(V_{tg} - V_{tg}^0)]/e$ and the displacement field $D = [C_{bg}(V_{bg} - V_{bg}^0) - C_{tg}(V_{tg} - V_{tg}^0)]/2\varepsilon_0$, respectively. This 2D diagram can be characterized into three dis-

tinct types of regions, which is significantly different from that of a conventional BLG parallel plate capacitor.[17] The first type of regions is located at the left and lower part of the diagram as well as at the top of the diagram (the triangular island in Figure 2a), where $C_{DUT} \approx C_G$, corresponding to highly conductive states of the sample with large carrier concentrations. The second type of regions is in the middle and right parts of the diagram, where $C_{DUT} \approx 0$, meaning that there is little charge carrier in this region, corresponding to a gapped state of the sample. These two types of regions exhibit features that are highly consistent with the resistance maps of similar BLG-CrOCl devices,[3] which

**ADVANCED
SCIENCE NEWS**

www.advancedsciencenews.com

**ADVANCED
MATERIALS**

www.advmat.de
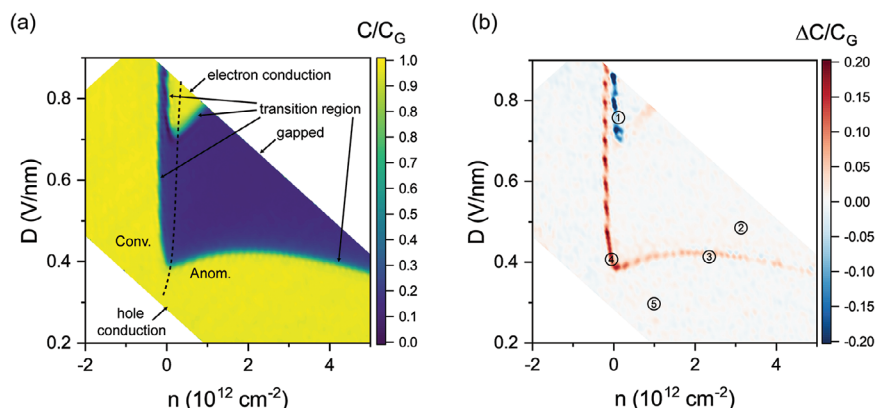
Figure 2. Quantum capacitance and capacitance hysteresis map of BLG-CrOCl. a) Dual gate map of capacitance at $B_\perp = 3T$ and $T = 2K$. The dashed line indicates a boundary of conventional part (Conv.) and anomalous part (Anom.) of the phase diagram. b) Dual gate map of capacitance hysteresis ($\Delta C = C_{DUT}(6T \rightarrow 3T) - C_{DUT}(0T \rightarrow 3T)$) at $B_\perp = 3T$ and $T = 2K$. Typical magnetic hysteresis curves at marked positions are shown in Figure 3a.

corroborate our conclusion about these two regions. The third type of regions is the focus of this article, which is defined to be the transition between the insulating states and the conductive states of the sample. This transition region is difficult to be characterized by resistance measurements but ideally suited for the precision capacitance measurement technique. In the following, we will discuss these three types of regions one-by-one, i.e., the conductive region, the gapped region, and the transition region.
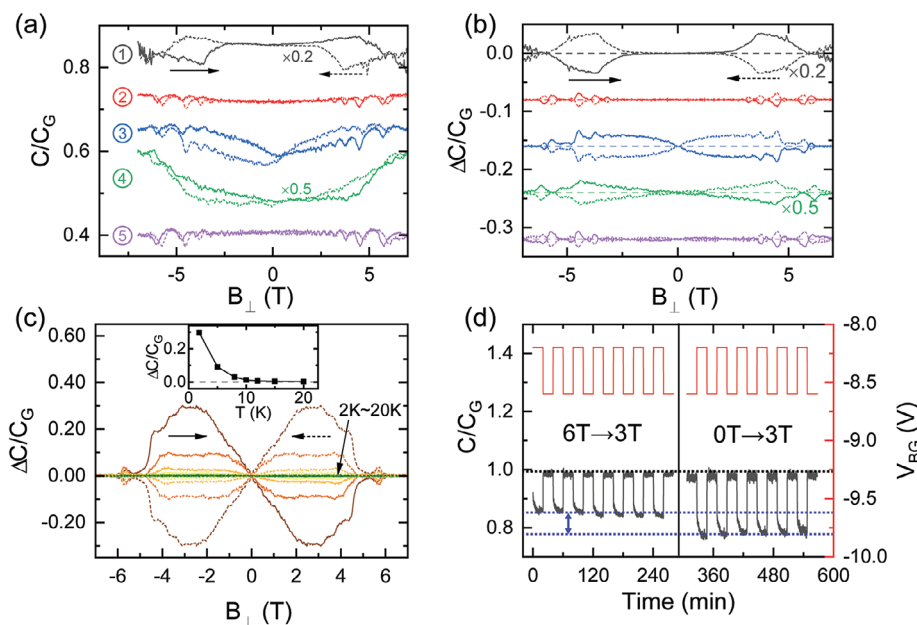
A black dashed line is drawn in Figure 2a, and it will become clear later that conventional behavior of the BLG-CrOCl heterostructure presents approximately to the left of this line, while anomalous behavior emerges to the right of it. This phenomenon has also been shown in resistance measurement[3] to be a result of the displacement field D tunable charge transfer between the BLG and CrOCl, causing an effective exchange of the role of n_{total} and D. Such effect creates a large hole conductive region at the lower part of the diagram, as well as a reduced triangular-shaped electron conductive region. Simply speaking, for $n_{total} < 0$ with all the experimentally explored D, the overall charge carrier type in the system is hole, and there are no charge transfer occurring between BLG and CrOCl; with $n_{total} > 0$, and with appropriate displacement field (e.g., $D < \approx 0.7$ V nm^{-1} in this particular device shown in Figure 2a), the valence band edge of CrOCl has lower energy than that of the conduction band edge of BLG, which causes most electrons in the BLG to be transferred to CrOCl, leaving holes or zero carrier density in BLG; with $n_{total} > 0$ and large enough D (e.g., $D > \approx 0.7$ V nm^{-1} in this particular device), such charge transfer process can be prohibited which enables the emergence of an electron conductive island in the phase diagram.[3] Based on our first-principles calculations, the energy difference between the electron band edge in BLG and AFM CrOCl is 0.78 eV (details in Experimental Section), the experimentally determined $D \approx 0.7$V/nm to drag electrons from CrOCl to BLG indicates an average charge transfer distance of ≈ 1.1 nm. Since the calculated average BLG-CrOCl distance is 3 Å and the CrOCl interlayer distance is 7 Å,[18] this charge transfer distance suggests that electrons transferred to CrOCl are mainly distributed on the topmost interfacial layer of the crystal. Early first-principles calculations have confirmed the existence of extensive charge transfer between graphene and CrOCl.[19] We

checked the 5×4 2L-CrOCl/$8 \times 3\sqrt{3}$ bilayer-graphene supercell to confirm that there is indeed electron transfer from bilayer graphene to AFM CrOCl, at a density of 0.047 electron/nm^2 (see Figures S9 and S10, Supporting Information).

The above discussion provides insight into the anomalous insulating state at the right part of the phase diagram, where a highly uniform gapped state is detected. The shape of this gapped state is consistent with the anomalous insulating state detected by resistance measurement.[3] A previous study indicated that electrons injected onto the top surface of CrOCl formed a long-wavelength charge order, promoting electron–electron (e–e) interactions in BLG via long-range Coulomb coupling.[20] This conclusion is in line with our data, since no mobile carrier is detected inside the gapped region by capacitance measurement (Figure 2a), proving that: 1) this gap is not a mobility gap, but a real energy bandgap; 2) the homogeneity of the gap goes far beyond what could be achieved in conventional dual-gated BLG devices.[3,21]

2.3. Magnetically Tunable Charging State Hysteresis in BLG-CrOCl

The previous section discussed the conductive regions and the gapped regions shown in Figure 2a, and we now turn to the discussion of the key findings of this article: the behavior of the DOS of BLG during the transition between these two regions under different history of the perpendicular magnetic field $B_\perp$. Under the application of $B_\perp$, the gapped region remain featureless and bent Landau levels emerges in the conductive regions (Figure S3, Supporting Information), similar to the results of resistance measurement;[3] remarkably, the DOS of the transition region is found to be intricately dependent on the history of magnetization of the heterostructure but not the history of electrical polarization or electrical doping. Figure 2b shows the capacitance difference $\Delta C_{DUT}(3T) = C_{DUT}(6T \rightarrow 3T) - C_{DUT}(0T \rightarrow 3T)$ measured at $B_\perp = 3$ T and $T = 2$ K. Here, $C_{DUT}(6T \rightarrow 3T)$ corresponds to C_{DUT} measured at $B_\perp = 3$ T with the device previously held at $B_\perp = 6$ T before $B_\perp$ ramps down to 3 T; similarly, $C_{DUT}(0T \rightarrow 3T)$ corresponds to C_{DUT} measured under $B_\perp = 3$ T

ADVANCED
SCIENCE NEWS

www.advancedsciencenews.com

ADVANCED
MATERIALS

www.advmat.de

Figure 3. Capacitance hysteresis loop and switching behavior of BLG-CrOCl. a) Capacitance and b) anti-symmetrized capacitance hysteresis in opposite magnetic field sweeping of BLG-CrOCl at marked positions of Figure 2b. The curves are shifted and scaled for clarity. c) Temperature dependence of capacitance hysteresis at position ③ of Figure 2b. The temperature ranges from 2 K (brown) to 20 K (green). Solid and dashed lines correspond to magnetic field sweeping up and down, respectively. Inset: temperature dependence of maximal capacitance hysteresis at $B_\perp = 3$ T. d) Switching behavior of BLG-CrOCl. BLG-CrOCl is switched in and out of the hysteretic area repeatedly at the positive field polarization (6T→3T) and zero field polarization (0T→3T) case, respectively. The nonvolatile charging states (marked by the two blue dashed lines) are found to be stable against the history of electrical gating.

with the device previously held at 0 T before $B_\perp$ ramps up to 3 T. Note that $B_\perp = 3$ T is chosen because ΔC_{DUT} is maximized at this magnetic field experimentally; this magnetic field value also co-incides with the antiferromagnetic (AFM) to ferrimagnetic (FiM) phase transition of CrOCl (Figure 1c).[22]

Figure 2b shows that $\Delta C_{DUT}(3T) = 0$ in most areas of the phase diagram, i.e., no hysteresis is detected due to the magnetization history of the sample. Interestingly, in the transition region, a finite signal was detected, i.e., $\Delta C_{DUT}(3T) \neq 0$, revealing a mag-netically controlled non-volatile charging state of the BLG-CrOCl heterostructure. This transition region can be divided into four segments: 1) the hole conductive state to gapped state transition in the conventional part (marked as segment I in Figure 2b); 2) the electron conductive state to gapped state transition in the conventional part (segment II); 3) the hole conductive state to gapped state transition in the anomalous part (segment III); and 4) the electron conductive state to gapped state transition in the anomalous part (segment IV). We found $\Delta C_{DUT}(3T) > 0$ in seg-ments I, III, and IV, while $\Delta C_{DUT}(3T) < 0$ in segment II. The hysteresis phenomenon can also be observed in our MHz capac-itance measurements (see Figure S7, Supporting Information).

To better understand the behavior of such hysteresis, we selected five representative points in the phase diagram in Figure 2b and examined C_{DUT} versus $B_\perp$ over a larger range of magnetic fields. Here, points ①, ③, and ④ are located in the area where $\Delta C_{DUT}(3T) \neq 0$, and points ② and ⑤ are located in the area where $\Delta C_{DUT}(3T) = 0$. **Figure 3a** shows C_{DUT} versus $B_\perp$ between -6 T and 6 T in two sweeping directions for points ① to ⑤. Dif-ferent field sweeping speeds were also tested to ensure that the

sweeping rate did not cause unwanted distortion of the signal (see Figure S5, Supporting Information). One can find that for points ①, ③, and ④, peculiar hysteresis loops emerge with maxima near $B_\perp = \pm3$ T; for points ② and ⑤, on the other hand, the C_{DUT} versus $B_\perp$ curves for the two sweeping directions overlap with each other, showing no hysteresis. The slight asymmetry between positive and negative magnetic fields might be due to magnetic domains and imperfections[23] and does not change our conclu-sions. Thus, we removed the slight asymmetry by first calculat-ing the difference in C_{DUT} between the up- and down- sweeping curves:

$$\tilde{\Delta}C_{DUT,up}\left(B_\perp\right) \equiv C_{DUT,up}\left(B_\perp\right) - C_{DUT,down}\left(B_\perp\right) \quad (2)$$

$$\tilde{\Delta}C_{DUT,down}\left(B_\perp\right) \equiv C_{DUT,down}\left(B_\perp\right) - C_{DUT,up}\left(B_\perp\right) \quad (3)$$

For $B_\perp = [-6$ T, 6 T]. Then, these two curves are anti-symmetrized and labeled as $\Delta C_{DUT,down}(B_\perp)$ and $\Delta C_{DUT,up}(B_\perp)$, respectively. Note that $\Delta C_{DUT,down}(B_\perp) \equiv -\Delta C_{DUT,up}(B_\perp)$ by defi-nition, thus any one of the curves will suffice in describing the behavior at point ① to ⑤; nonetheless, we plot both Equations (2) and (3) in Figure 3b to better illustrate the hysteresis. The sizable hysteresis in these curves is possibly related to metastable states in CrOCl between the two ground states at 0 and ±6T.[22c]

Figure 3c shows a typical temperature dependence of the hys-teresis at point ③. The inset shows maximal capacitance hys-teresis $\Delta C_{DUT,down}(3T)$ versus temperature, exhibiting an onset of the hysteresis at ≈12 K, consistent with the Néel tempera-ture of CrOCl.[22b] This indicates that the hysteresis in DOS of

ADVANCED
SCIENCE NEWS

www.advancedsciencenews.com

**ADVANCED
MATERIALS**

www.advmat.de
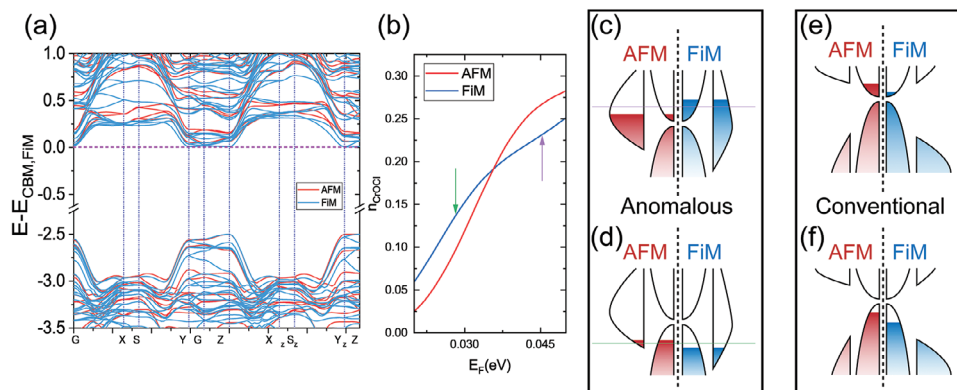
Figure 4. DOS of CrOCl and band alignment of BLG- CrOCl heterostructure. a) Calculated band structure of bulk CrOCl at AFM and FiM states, respectively. Zero energy is defined to be at the conduction band edge of CrOCl at the FiM state. b) Electron density of CrOCl conduction band as a function of energy near the crossing point right above the conduction band edge. c,d) Illustration of band alignment of BLG-CrOCl heterostructure at c) electron conduction and d) hole conduction within the anomalous part of the phase diagram in Figure 2a; e,f) Illustration of band alignment of BLG-CrOCl heterostructure at e) electron conduction and f) hole conduction within the conventional part of the phase diagram in Figure 2a. In Figure 4c–f, the parabolic bands in the middle of the panels (near the vertical black broken lines) represent BLG bands and the other bands located to the left and right of the BLG bands are the energy bands of CrOCl at the AFM state and the FiM state, respectively. For each figure in (c–f), the filled bands mark by red has the same area as the filled bands marked by blue, meaning the total number of electrons/holes of the heterostructure are equal in both the AFM and FiM states. The purple and green lines in (c,d) indicate Fermi energy positions marked by the purple and green arrows in (b), respectively.

the BLG is controlled by the magnetic order of the CrOCl substrate and likely not by the gate electric field. To further verify this hypothesis, we measured the hysteresis of the charging state against electrostatic gating. The upper section of Figure 3d displays the repeated switching of the back gate voltage V_{BG} between −8.2 and −8.6 V, with a fixed top gate voltage V_{TG} = 15 V, and the lower section shows the respective changes in the reduced device capacitance C_{DUT}/C_G. This operation is to tune the BLG-CrOCl heterostructure repeatedly from the hole conductive region to the transition region, near point ③ in Figure 2a. Specifically, the left panel of Figure 3d shows $C_{DUT}(6T{\rightarrow}3T)$, and the right panel shows $C_{DUT}(0T{\rightarrow}3T)$ under the same electrostatic tuning via the repeated switching of V_{BG}. As shown in Figure 3d, in both the 6T→3T state and the 0T→3T state, the switching of V_{BG} results in highly repeatable capacitances in the conductive region (black dashed line); however, in the transition region (two blue dashed lines), the capacitance is clearly dependent on the history of magnetization. A clear difference between the achieved C_{DUT} of the 6T→3T state and the 0T→3T state is marked by the two blue dashed lines in Figure 3d, which is not dependent on the history of electrostatic gating.

3. Discussion

To understand the physical origin of the magnetically tunable hysteresis in the charging states of the BLG-CrOCl heterostructures, we performed first-principles calculations on the energy bands of CrOCl in both the AFM and FiM magnetic states. **Figure 4a** shows the calculated energy bands for both magnetic states, which are aligned at their vacuum energies (details in Experimental Section), and zero energy is defined to be the conduction band edge of the FiM state. Note that the band gap of the FiM state is 2.50 eV, slightly smaller than that of the AFM state (2.55 eV). The DOS of CrOCl DOS_{CrOCl} versus Fermi energy E_F between 0 and 0.045 eV are shown in Figure S8b (Support-

ing Information). The accumulated electron number of CrOCl starting from the conduction band edge up to the Fermi energy is defined as $n_{CrOCl}(E_F) = \int_0^{E_F} DOS_{CrOCl}(E)dE$, and $n_{CrOCl}(E_F)$ for E_F ranging between 0.015 and 0.05 eV is shown in Figure 4b. In the experimentally explored parameters, we only observed transfers of electrons from BLG to CrOCl, and not hole from BLG to CrOCl, thus the charge transfer physics is happening around the conduction band edge of the CrOCl substrate, and not around the valence band edge of CrOCl, meaning $n_{CrOCl} \geq 0$.

When $n_{total} > 0$ and $n_{CrOCl} > 0$, the total accumulated charge in the BLG-CrOCl heterostructure is electrons and the Fermi level is above the conduction band edge of CrOCl, this corresponds to the anomalous part of the phase diagram in Figure 2b, and a substantial number of electrons are transferred from the BLG to the surface of CrOCl and then localized by electron–electron interactions.[3] Within this regime, Figure 4b shows that the accumulated electron number in the CrOCl crystal has a crossing point, such that $|n_{CrOCl}|_{FiM} > |n_{CrOCl}|_{AFM}$ below the crossing point and $|n_{CrOCl}|_{FiM} < |n_{CrOCl}|_{AFM}$ above the crossing point. Since $n_{BLG} = n_{total} - n_{CrOCl}$, it implies that $|n_{BLG}|_{FiM} > |n_{BLG}|_{AFM}$ for both electron conduction (around the E_F value indicated by the purple arrow) and hole conduction (around the E_F value indicated by the green arrow) in the BLG with proper band alignment, resulting in the anomalous behavior of $\Delta C_{DUT}(3T) > 0$ in both segments III and IV in the anomalous part of the phase diagram in Figure 2b. With the above discussion, the present study provides an example of magnetically controlled charging states in 2D van der Waals heterostructures. This mechanism can be universally extended to the cross-control of the electric and magnetic states of interfacial matter.

When $n_{CrOCl} = 0$, the Fermi level of the heterostructure is inside the band gap of CrOCl, which corresponds to the conventional part of the phase diagram in Figure 2b. In this part, we observed a consistent upshift of the Fermi energy of the BLG

**ADVANCED
SCIENCE NEWS**

www.advancedsciencenews.com

**ADVANCED
MATERIALS**

www.advmat.de

channel when changing the magnetic state of CrOCl from FiM state to AFM state. This behavior is not related to the correlated behavior of the BLG-CrOCl heterostructure in the charge transfer region and is likely caused by a more conventional physical effect, which is the magnetically tunable mid-gap states. In this situation, the charge transfer between BLG and CrOCl only serves to fill the valance band of CrOCl and the possible mid-gap states of CrOCl. In magnetic semiconductors, the mid-gap states can be modulated by the magnetic configuration, wherein distinct magnetic states induce variations in the energy levels of the mid-gap states.[24] Such variation will result in a consistent shift of the Fermi energy in the BLG regardless of its carrier type, giving rise to the change of sign in the $\Delta C_{DUT}(3T)$ signal for electron and hole conduction in BLG. The situation is illustrated in Figure 4e,f: for hole doping (Figure 4f), the carrier density of BLG with CrOCl in the FiM state is *larger* than that with CrOCl in the AFM state, i.e., $|n_{BLG,h}|_{CrOClFiM} > |n_{BLG,h}|_{CrOClAFM}$; whereas for electron doping (Figure 4e), the carrier density of BLG with CrOCl in the FiM state is *smaller* than that with CrOCl in the AFM state, i.e., $|n_{BLG,e}|_{CrOClFiM} < |n_{BLG,e}|_{CrOClAFM}$. Thus, $\Delta C_{DUT}(3T) \propto [|n_{BLG}|_{CrOClFiM} - |n_{BLG}|_{CrOClAFM}] > 0$ in segment I and $\Delta C_{DUT}(3T) < 0$ in segment II. Note that such mid-gap states are sample dependent, so that the transition region at the conventional part does not necessarily have the same strength of hysteresis for different CrOCl crystals (see Figure S5, Supporting Information).

4. Summary

To summarize, we investigated the quantum capacitance of bilayer graphene-CrOCl heterostructures, revealing a unique non-volatile state that can be synergetically controlled via magnetic-electrical means. The temperature, electrical field and magnetic field dependence of this non-volatile state linked this effect to the magnetic phase transition of CrOCl between the AFM and FiM phases. Based on first-principles calculations, we proposed that such non-volatile state is due to the magnetically tuned charge transfer between the bilayer graphene and CrOCl. Our work provides the first evidence of magnetically related behavior in BLG-CrOCl heterostructures; it also reveals a new route to construct novel van der Waals interfaces with non-volatile and cross-parameter controls for data storage and processing in future information technology.

5. Experimental Section

Device Fabrication: The BLG/CrOCl heterostructures were assembled using a standard dry transfer method.[25] The materials used for the device were first exfoliated onto Si substrates with a 295 nm thick SiO$_2$ layer. A polycarbonate (PC) stamp was used to pick up the top h-BN flake, thin graphite contact, bilayer graphene, bottom CrOCl flake, and thin graphite gate in sequence. Two pieces of graphite were used to electrically connect the bilayer graphene and metal electrodes, ensuring stable electrical contact at low temperature. The PC stamp with the heterostructure was heated to 90–150 °C during pick-up and to 180 °C to drop on a polished sapphire device substrate, which was used to reduce parasitic capacitance. Finally, the PC was dissolved in chloroform at room temperature. Standard electron beam lithography (EBL) and metal deposition techniques (Ti 5 nm/Au 50 nm) were then used to contact the thin graphite and define the top gate electrode, forming a heterostructure parallel plate capacitor device.

Capacitance Measurements: The capacitance between the graphene sheet and the graphite back gate was measured using a low-temperature capacitance bridge based on an FHX35X high-electron mobility transistor (HEMT). The sample capacitance C_{DUT} and the standard capacitance C_R were both connected with the HEMT gate as a common point. The HEMT acts as an amplifier and improves the signal-to-noise ratio.[11d] By applying a constant amplitude AC excitation V_x to the sample and adjusting the AC excitation V_{REF} to the standard capacitor, a V-shaped curve of the output voltage could be obtained. V_x has an amplitude of 10 mV to avoid gating the sample and was ≈180° out of phase with respect to V_{REF}. The measured C_{DUT} is independent of frequencies ranging from 1370 to 8370 Hz (Figure S2, Supporting Information). The measurement frequency in the main text is 5370 Hz. By using feedback control V_{REF}, the circuit is kept at the balanced point, where the amplitude of the output voltage is minimal. The sample capacitance is then given by

$$C_{DUT} = \left(\frac{V_{REF}}{V_X}\right) C_R \tag{4}$$

The total measured capacitance between the bottom gate and BLG is given by

$$C_{DUT} = \left(\frac{1}{C_G} + \frac{1}{C_Q}\right)^{-1} + C_P \tag{5}$$

where $C_G = \frac{\varepsilon_r \varepsilon_0 S}{d}$ is the geometric capacitance, $C_Q = \frac{Ae^2 dn}{d\mu}$ is the quantum capacitance, and C_P is the parasitic capacitance due to the coaxial cable and stray capacitances. The parasitic capacitance is estimated by subtracting the geometric capacitance from the total capacitance measured when the sample is in a metallic state, where $C_Q \gg 1$.

First-Principles Calculations: The DFT calculations were performed using the generalized gradient approximation for the exchange-correlation potential, the projector augmented wave method,[26] and a plane-wave basis set as implemented in the Vienna ab initio simulation package (VASP).[27] Dispersion correction was performed at the van der Waals density functional (vdW-DF) level,[28] with the optB86b functional for the exchange potential,[29] which was proven to be accurate in describing the structural properties of layered materials[30] and was adopted for structure-related calculations. The shape and volume of each supercell and all atomic positions of CrOCl bulks were fully relaxed until the residual force per atom was $<1 \times 10^{-3}$ eV·Å^{-1} in the calculations. In the VASP calculations, the kinetic energy cutoff for the plane-wave basis set was set to be 700 eV for the geometric and electronic structure calculations. A k-mesh of $10 \times 14 \times 4$ was adopted to sample the first Brillouin zone of the conventional unit cell of the CrOCl bulk. The on-site Coulomb interactions with the Cr d orbitals had U and J values of 3.0 and 1.0 eV, respectively, as revealed by a linear response method[26] and comparison with the experimental results.[22b] These values are comparable to those adopted in modeling CrSCl[31] and CrI$_3$.[32] For calculations of mono- and fewlayer CrOCl, a sufficiently large vacuum layer over 20 Å along the out-of-plane direction was adopted to eliminate interactions among the monolayers. Considering the valence band edge of −5.89 eV (−5.87 eV) for AFM (FiM) CrOCl and the work function of 5.11 eV for bilayer graphene in the CrOCl vdW heterostructure, electrons may transfer readily from graphene to CrOCl. To consider the interfacial charge transfer, a 5×4 CrOCl/$8 \times 3\sqrt{3}$ bilayer graphene supercell and a 5×15 CrOCl/$8 \times 11\sqrt{3}$ bilayer graphene supercell were developed for calculations of interfacial differential charge densities of CrOCl in the antiferromagnetic (AFM) and ferrimagnetic (FiM) phases, respectively (Figures S9 and S10, Supporting Information).

Supporting Information

Supporting Information is available from the Wiley Online Library or from the author.

Conflict of Interest

The authors declare no conflict of interest.

Author Contributions

S.C., R.Z., and C.W. contributed equally to this work. J.-H.C., Z.H., and Y.Y. conceived the idea and designed the experiments. S.C., R.Z., and Y.W. fabricated the devices. S.C. and R.Z. performed the magneto-transport measurements with the help of N.M., M.C., Y.L, Y.S., Y.F., T.H., and Y.Z.; C.W. performed the calculations. P.G provided CrOCl crystal. K.W. and T.T. provided hexagonal boron nitride crystal. J.-H.C., Z.H. X.C.X., W.J., and Y.Y., analyzed the data. J.-H.C., R.Z, S.C., and C.W. wrote the paper with the input from all the authors.

Data Availability Statement

The data that support the findings of this study are available from the corresponding author upon reasonable request.

[1] H. Schäfer, F. Wartenpfuhl, *März* **1961**, *308*, 282.
[2] Y. Wang, X. Gao, K. Yang, P. Gu, X. Lu, S. Zhang, Y. Gao, N. Ren, B. Dong, Y. Jiang, K. Watanabe, T. Taniguchi, J. Kang, W. Lou, J. Mao, J. Liu, Y. Ye, Z. Han, K. Chang, J. Zhang, Z. Zhang, *Nat. Nanotechnol.* **2022**, *17*, 1272.
[3] K. Yang, X. Gao, Y. Wang, T. Zhang, Y. Gao, X. Lu, S. Zhang, J. Liu, P. Gu, Z. Luo, R. Zheng, S. Cao, H. Wang, X. Sun, K. Watanabe, T. Taniguchi, X. Li, J. Zhang, X. Dai, J. H. Chen, Y. Ye, Z. Han, *Nat. Commun.* **2023**, *14*, 2136.
[4] Y. Guo, J. Li, X. Zhan, C. Wang, M. Li, B. Zhang, Z. Wang, Y. Liu, K. Yang, H. Wang, W. Li, P. Gu, Z. Luo, Y. Liu, P. Liu, B. Chen, K. Watanabe, T. Taniguchi, X.-Q. Chen, C. Qin, J. Chen, D. Sun, J. Zhang, R. Wang, J. Liu, Y. Ye, X. Li, Y. Hou, W. Zhou, H. Wang, et al., *Nature* **2024**, *630*, 346.
[5] T. Zhang, Y. Wang, H. Li, F. Zhong, J. Shi, M. Wu, Z. Sun, W. Shen, B. Wei, W. Hu, X. Liu, L. Huang, C. Hu, Z. Wang, C. Jiang, S. Yang, Q. M. Zhang, Z. Qu, *ACS Nano* **2019**, *13*, 11353.
[6] P. Gu, Y. Sun, C. Wang, Y. Peng, Y. Zhu, X. Cheng, K. Yuan, C. Lyu, X. Liu, Q. Tan, Q. Zhang, L. Gu, Z. Wang, H. Wang, Z. Han, K. Watanabe, T. Taniguchi, J. Yang, J. Zhang, W. Ji, P. H. Tan, Y. Ye, *Nano Lett.* **2022**, *22*, 1233.
[7] J. Angelkort, A. Wölfel, A. Schönleber, S. van Smaalen, R. K. Kremer, *Phys. Rev. B* **2009**, *80*, 144416.
[8] X. Zhang, Y. Guo, Z. Zhou, X. Zhang, Y. Chen, X. C. Zeng, J. Wang, *Adv. Funct. Mater.* **2022**, *32*, 2200154.
[9] Y. Wang, J. Balgley, E. Gerber, M. Gray, N. Kumar, X. Lu, J.-Q. Yan, A. Fereidouni, R. Basnet, S. J. Yun, D. Suri, H. Kitadai, T. Taniguchi, K. Watanabe, X. Ling, J. Moodera, Y. H. Lee, H. O. H. Churchill, J. Hu, L. Yang, E.-A. Kim, D. G. Mandrus, E. A. Henriksen, K. S. Burch, *Nano Lett.* **2020**, *20*, 8446.
[10] L. Wang, I. Meric, P. Y. Huang, Q. Gao, Y. Gao, H. Tran, T. Taniguchi, K. Watanabe, L. M. Campos, D. A. Muller, J. Guo, P. Kim, J. Hone, K. L. Shepard, C. R. Dean, *Science* **2013**, *342*, 614.
[11] a) R. C. Ashoori, H. L. Stormer, J. S. Weiner, L. N. Pfeiffer, S. J. Pearton, K. W. Baldwin, K. W. West, *Phys. Rev. Lett.* **1992**, *68*, 3088; b) A. F. Young, C. R. Dean, I. Meric, S. Sorgenfrei, H. Ren, K. Watanabe, T. Taniguchi, J. Hone, K. L. Shepard, P. Kim, *Phys. Rev. B* **2012**, *85*, 235458; c) A. A. Zibrov, C. Kometter, H. Zhou, E. M. Spanton, T. Taniguchi, K. Watanabe, M. P. Zaletel, A. F. Young, *Nature* **2017**, *549*, 360; d) T. Li, J. Zhu, Y. Tang, K. Watanabe, T. Taniguchi, V. Elser, J. Shan, K. F. Mak, *Nat. Nanotechnol.* **2021**, *16*, 1068.
[12] a) G. L. Yu, R. Jalil, B. Belle, A. S. Mayorov, P. Blake, F. Schedin, S. V. Morozov, L. A. Ponomarenko, F. Chiappini, S. Wiedmann, U. Zeitler, M. I. Katsnelson, A. K. Geim, K. S. Novoselov, D. C. Elias, *Proc. Natl. Acad. Sci. USA* **2013**, *110*, 3282; b) B. Guo, A. C. Lygo, X. Dai, S. Stemmer, *APL Mater.* **2022**, *10*, 091116; c) F. Xiu, N. Meyer, X. Kou, L. He, M. Lang, Y. Wang, X. Yu, A. V. Fedorov, J. Zou, K. L. Wang, *Sci. Rep.* **2012**, *2*, 669.
[13] M. Kuiri, C. Kumar, B. Chakraborty, S. N. Gupta, M. H. Naik, M. Jain, A. K. Sood, A. Das, *Nanotechnology* **2015**, *26*, 485704.
[14] A. F. Young, J. D. Sanchez-Yamagishi, B. Hunt, S. H. Choi, K. Watanabe, T. Taniguchi, R. C. Ashoori, P. Jarillo-Herrero, *Nature* **2014**, *505*, 528.
[15] T. Li, S. Jiang, B. Shen, Y. Zhang, L. Li, Z. Tao, T. Devakul, K. Watanabe, T. Taniguchi, L. Fu, J. Shan, K. F. Mak, *Nature* **2021**, *600*, 641.
[16] a) L. Ma, P. X. Nguyen, Z. Wang, Y. Zeng, K. Watanabe, T. Taniguchi, A. H. MacDonald, K. F. Mak, J. Shan, *Nature* **2021**, *598*, 585; b) Y. Cao, V. Fatemi, A. Demir, S. Fang, S. L. Tomarken, J. Y. Luo, J. D. Sanchez-Yamagishi, K. Watanabe, T. Taniguchi, E. Kaxiras, R. C. Ashoori, P. Jarillo-Herrero, *Nature* **2018**, *556*, 80.
[17] M. Kuiri, A. Das, *Phys. Rev. B* **2019**, *99*, 125411.
[18] N. Miao, B. Xu, L. Zhu, J. Zhou, Z. Sun, *J. Am. Chem. Soc.* **2018**, *140*, 2417.
[19] B. Ying, B. Xin, M. Li, S. Zhou, Q. Liu, Z. Zhu, S. Qin, W.-H. Wang, M. Zhu, *ACS Appl. Mater. Interfaces* **2024**, *16*, 43806.
[20] X. Lu, S. Zhang, Y. Wang, X. Gao, K. Yang, Z. Guo, Y. Gao, Y. Ye, Z. Han, J. Liu, *Nat. Commun.* **2023**, *14*, 5550.
[21] R. T. Weitz, M. T. Allen, B. E. Feldman, J. Martin, A. Yacoby, *Science* **2010**, *330*, 812.
[22] a) M. Zhang, Q. Hu, Y. Huang, C. Hua, M. Cheng, Z. Liu, S. Song, F. Wang, H. Lu, P. He, G. H. Cao, Z. A. Xu, Y. Lu, J. Yang, Y. Zheng, *Small* **2023**, *19*, 2300964; b) P. Gu, Y. Sun, C. Wang, Y. Peng, Y. Zhu, X. Cheng, K. Yuan, C. Lyu, X. Liu, Q. Tan, Q. Zhang, L. Gu, Z. Wang, H. Wang, Z. Han, K. Watanabe, T. Taniguchi, J. Yang, J. Zhang, W. Ji, P.-H. Tan, Y. Ye, *Nano Lett.* **2022**, *22*, 1233; c) P. Gu, C. Wang, D. Su, Z. Dong, Q. Wang, Z. Han, K. Watanabe, T. Taniguchi, W. Ji, Y. Sun, Y. Ye, *Nat. Commun.* **2023**, *14*, 3221.

**ADVANCED
SCIENCE NEWS**

www.advancedsciencenews.com

**ADVANCED
MATERIALS**

www.advmat.de

[23] C. Cao, X. Liu, X. Ren, X. Zeng, K. Zhang, D. Sun, S. Zhou, Y. Wu, Y. Li, J.-H. Chen, *2D Mater.* **2018**, *5*, 044003.

[24] a) J. J. Chen, H. C. Wu, D. P. Yu, Z. M. Liao, *Nanoscale* **2014**, *6*, 8814; b) D. Cao, B. Liu, H. Yu, W. Hu, M. Cai, *Eur. Phys. J. B* **2015**, *88*, 75; c) X. Hou, M. Wumiti, S. Kumar, K. Shimada, M. Sawada, *Appl. Surf. Sci.* **2022**, *594*, 153416.

[25] L. Wang, I. Meric, P. Y. Huang, Q. Gao, Y. Gao, H. Tran, T. Taniguchi, K. Watanabe, L. M. Campos, D. A. Muller, J. Guo, P. Kim, J. Hone, K. L. Shepard, C. R. Dean, *Science* **2013**, *342*, 614.

[26] G. Kresse, D. Joubert, *Phys. Rev. B* **1999**, *59*, 1758.

[27] G. Kresse, J. Furthmüller, *Comp. Mater. Sci.* **1996**, *6*, 15.

[28] M. Dion, H. Rydberg, E. Schröder, D. C. Langreth, B. I. Lundqvist, *Phys. Rev. Lett.* **2004**, *92*, 246401.

[29] J. Klimeš, D. R. Bowler, A. Michaelides, *Phys. Rev. B* **2011**, *83*, 195131.

[30] J. Qiao, Y. Pan, F. Yang, C. Wang, Y. Chai, W. Ji, *Sci. Bull.* **2018**, *63*, 159.

[31] C. Wang, X. Zhou, L. Zhou, N.-H. Tong, Z.-Y. Lu, W. Ji, *Sci. Bull.* **2019**, *64*, 293.

[32] P. H. Jiang, C. Wang, D. C. Chen, Z. C. Zhong, Z. Yuan, Z. Y. Lu, W. Ji, *Phys. Rev. B* **2019**, *99*, 144401.